

Theoretical Investigations of Transition-Metal Surface Energies under Lattice Strain and CO Environment

Michael T. Tang^{1,2}, Zachary W. Ulissi³, and Karen Chan^{*2}

¹SUNCAT Center for Interface Science and Catalysis, Department of Chemical Engineering, Stanford University, Stanford, California 94305

²SUNCAT Center for Interface Science and Catalysis, SLAC National Accelerator Laboratory, Menlo Park, California 94025

³Department of Chemical Engineering, Carnegie Mellon University, Pittsburgh, Pennsylvania 15213

**Corresponding author's email: chank@slac.stanford.edu*

June 6, 2018

Abstract

An understanding of the relative stability of surface facets is crucial in order to develop predictive models of catalyst activity and to fabricate catalysts with controlled morphology. In this work, we present a systematic density functional theory (DFT) study of the effect of lattice strain and of a CO environment on the surface formation energies of Cu, Pt, and Ni. First, we show both compressive and tensile lattice strain favors the formation of stepped vs. low-index terraces such as (111) and (100). Then, we investigate the effect of a CO environment using configurations of CO at various coverages, determined using a greedy, systematic approach, inspired by forward stepwise feature selection. We find that a CO environment favors stepped facets on Ni, Cu and Pt. These trends are illustrated with the corresponding equilibrium Wulff shapes at various strain and CO pressures. In general, the surface energies of the studied transition metals are highly sensitive to strain and CO coverage, which should be considered when rationalizing trends in catalytic activity.

1 Introduction

The majority of commercial transition metal catalysts are polycrystalline, with catalytic activity that is highly dependent on the facet and coordination of the active sites. The relative stability of various facets are sensitive to external factors, such as lattice strain or the presence of adsorbates. When the bonds of atoms are stretched or compressed, their electronic structure also changes. In the case of metallic systems, the d-band center shifts down or up as the orbitals become less overlapped with stretching or more overlapped with compression, respectively^{1,2}. Lattice strain is present in core-shell nanoparticles, overlayer or dealloyed films, or in cases where internal lattice mismatch is present, such as subsurface oxide structures or electroplated materials. These systems have been thoroughly exploited in catalyst development¹⁻¹³. Twinning defects within the nanoparticles may also cause lattice strain to appear on the surface¹⁴.

There exists extensive literature on surface reconstruction of transition metals in the presence of adsorbates, most notably: the Au or Pt(110) missing row reconstruction¹⁵, the Ni clockwise-rotated (100) reconstruction in the presence of CO¹⁶, or Cu (110)/(111) row reconstruction from O chemisorption^{17,18}. The presence of adsorbates can influence nanoparticle anisotropic growth through preferential adsorption onto certain facets¹⁹. There have also been reports that suggest surface reconstruction occurring under electrochemical conditions^{20,21}. These studies suggest that active catalytic surfaces during reactions are unlikely to be similar to their counterpart under ideal vacuum conditions. The extent of the structural change should be addressed in the development of a predictive theory of catalytic activity.

In this article, we provide a density functional theory study of the effect of lattice strain and CO coverage effects on the stability of 12 different facets on 3 transition metals commonly used in catalysis: Cu, Ni, and Pt. Generally we found lattice strain and CO coverage to increase the relative stability of stepped facets. We illustrate these trends with the corresponding Wulff particle shapes.

2 Methods

2.1 DFT Calculation Parameters

All electronic structure calculations were carried out via the open-source package Quantum ESPRESSO²², interfaced with the Atomic Simulation Environment²³. The exchange-correlation energies were approximated using the PBE generalized gradient approximation (GGA) functional and BEEF-vdW^{24,25} functional. The advantages of BEEF-vdW are that it includes a non-local van der Waals correction and is tailored to surface chemistry. PBE is the standard functional for the Crystallium Periodic Table database of surface energies, created for the Materials Project. The surface energy calculations of this database have been compared with experimental surface energies and found to be in close agreement within a 10% error²⁶. Thus, we benchmarked our calculations against Crystallium.

All slab calculations were performed using a plane-wave basis (plane-wave cutoff of 500 eV, density-wave cutoff of 5000 eV) and the Brillouin zone is sampled by a Monkhorst-Pack k -point mesh of (6,6,1)²⁷. Ultrasoft pseudopotentials were used for this study. Free energy contributions to gas phase CO are given by

$$\mu_{CO} = E_{CO} + E_{ZPE} + \int C_p dT + k_B T \ln \left(\frac{p}{p_o} \right) \quad (1)$$

and determined using standard ideal-gas methods[?]. Likewise the free energy contributions to adsorbed CO were determined using the vibrations from the harmonic approximation[?].

2.2 Slab Generation and Strain Application

We enumerated 12 different facets up to a maximum index of 3 for Ni, Pt, and Cu for our systematic study, which allows us to include an ensemble of possible stepped surfaces. The facets were translated into slab structures using a slab generation algorithm implemented in the Python Materials Genomics (pymatgen) materials analysis library²⁸.

All slab structures were created with a vacuum of at least 12 Å to ensure that no interaction of periodic slabs take place. To calculate surface energies, we generated slabs with three different thicknesses, ranging from 4 to 12 atomic layers in thickness. We fixed any atoms that were below the first layer to ensure there aren't any Poisson effects implicated in our slab relaxations²⁹.

Since we only consider face-centered cubic (FCC) structures, all slabs generated have a single termination and have symmetric top and bottom surfaces. For Pt only, we included the missing row reconstruction for (110), which was suggested by previous experimental and computational results¹⁵. A reconstructed (110) slab model is provided in as Supplementary Figure S2.

Biaxial lattice strain was applied by modifying the unit cell by a given percentage amount in the x and y direction. For this study, we apply up to 3% strain, where compressive strain is denoted as a negative value and tensile strain a positive one.

2.3 Surface Formation Energy Calculation Approach And Benchmark

We applied the linear-fit, intercept extrapolation method^{30?} for determining surface energy using DFT energies for slabs at three different thicknesses. This method mitigates the convergence issue that arises when k -points in bulk calculations and surface slab calculations do not line up³⁰, and allows for convergence of surface formation energies with as little as 3 different slab thickness calculations³⁰.

For a given slab exposed at the (hkl) plane with n atoms, its surface energy γ is given by

$$\gamma^{hkl} = (E_{slab}^{hkl} - E_{bulk} n_{slab}) / (2A_{slab}^{hkl}), \quad (2)$$

where A_{slab}^{hkl} is the cross-sectional area of the slab's unit cell, n_{slab} the number of atoms in the slab. E_{slab}^{hkl} the energy of the slab itself, and E_{bulk} the energy of optimized bulk structure per atom. To determine the intrinsic surface energy, we fit the energies of slabs of varying thicknesses to Eq. (3) and take the intercept corresponding to a slab thickness of zero. Therefore, the determined surface energy does not explicitly reference the bulk energy, since the errors associated with this energy have been shown to lead to a divergence in surface energies with increasing number of atomic layers[?]. Surface energies for all facets considered were converged with slab thicknesses of at least 10 atomic layers. Supplementary Figure S1 shows, as an example, the surface energy calculated with the linear-fit method for Ni(111). In addition, Table S1 in the Supplemental Information compares the unstrained Ni surface energies for both the PBE and BEEF exchange correlation functionals with the surface energies found on Crystallium. Overall, both PBE and BEEF give γ that agree very well with those of the Crystallium database. In our analysis, we focussed

on BEEF results. A similar analysis on lattice strain was performed in PBE and is provided in our Supplementary Information Table 1, 4-5, 8-9, 12-13, 15, which shows the same trends to hold for PBE as BEEF.

2.4 Wulff Construction

Surface energies were translated into equilibrium Wulff shapes using the Wulff construction:

$$\Delta G_i = \sum_j \gamma_j A_j \quad (3)$$

where γ_j is the surface energy per unit area of the j^{th} face, A_j is the area of that face, and ΔG_i is the Gibbs free energy difference between a real crystal with i atoms vs. the same number of atoms inside a hypothetical bulk crystal. From the Gibbs-Wulff theorem, the shape of minimum ΔG_i is determined by translating the facets from the crystal center by a distance proportional to their surface energies. Facets with high surface energies are translated a greater distance from the crystal center than facets with low surface energies. The resulting Wulff shape is enclosed by the smallest set of surfaces capable of covering the entire volume^{26,31}. Our unstrained Wulff shapes generally agree with those generated by the Crystallium database²⁶. We note that this approach does not account for growth or metastability kinetics, which can come into play especially at high temperatures and in the presence of surfactants³². Size dependent stress may also influence the morphology of nanoparticles³³.

2.5 Systematic Coverage Calculations

To systematically determine adsorbate configurations as a function of coverage, we employed a greedy forward-stepwise approach, inspired by the feature selection technique used in machine learning⁷. This approach allows us to estimate a reasonably low energy adsorbate configuration for the multiple surfaces examined in this paper, and bypass the use of minima-hopping³⁴, which attempts to find global minima at a given adsorbate coverage through a series of molecular dynamics and optimization steps³⁵. The greedy approach is as follows: the configurations considered for $n + 1$ adsorbates are determined by mapping out the sites still remaining from the lowest energy configuration found for n adsorbates. Thus, given s sites on the surface, we potentially consider $s(s + 1)/2 + 1$ possible adsorbate configurations. Depending on which atoms are considered as surface atoms, a 2x1 unit cell of a fcc(211) facet would then have 4 to 6 ontop sites, 8 bridge sites, and 4 to 8 hollow sites. A 2x2 unit cell of a fcc(111) has 4 ontop sites, 12 bridge sites, 8 hollow sites per cell. As the number of adsorbates increase, the number of possible sites that are examined decreases.

To implement this approach, we generalized the adsorption site finder in the Pymatgen python module²⁸. This adsorption site finder is capable of finding ontop, bridge, and hollow sites, given the bulk material and facet inputs. We have generalized the code such that: (1) it finds potential adsorption sites for any slabs we provide as input; (2) because adsorption sites are comprised of surface atoms, the algorithm will also log information about the surface atom(s) which comprise that site; this include cartesian coordinates of the atoms that make the site as well as the coordination number of the surface atoms. We utilize these new features to systematically search across surfaces for adsorption sites. These new features will be added to the adsorption module in a future version of Pymatgen.

We note that, due to the approach’s greedy nature, the algorithm is not guaranteed to obtain the lowest energy adsorbate configuration, since adsorbate-adsorbate interactions will modify the effective binding energies on the surfaces. Adsorbates on the surface may rearrange as more are added to the surface, such that a newly relaxed $n + 1$ adsorbate-covered structure deviates from the original n adsorbate-covered structure. Nevertheless, we find the expected trends in the evolution of adsorbate configurations with increasing coverage. At low coverage ($\theta \leq 0.25$), the adsorbates were found to bind more favorably at the step atom sites than terrace sites, due to the 0.2-0.3 eV difference binding energies between them. At moderate to high coverages, we found that the greedy approach will favor sites that are relatively equidistant to existing adsorbed intermediates, which minimize adsorbate-adsorbate repulsions. Thus, the approach, by and large, provides a systematic way to estimate the equilibrium adsorption coverage for a given adsorbate on a given surface, and with considerably less computing time than minima hopping.

For all 3 metals, the coverage calculations were done on 10 of the 12 facets considered for the strain effect. We did not consider (322) and (332) in our coverage calculations, since they contain a considerably larger variety of sites. Due to the variety in adsorbate-adsorbate interactions that are possible, systematic coverage calculations would be considerably more computationally expensive. We do not expect that the general trend of the stabilization of steps or more undercoordinated facets by CO to be affected by this omission. The slabs used were at least 4 atoms thick. The atoms of the adsorbates and the first surface layer were allowed to freely move about, while the bulk layers were fixed. We considered coverages on 2x1 cells for stepped facets, and 2x2 cells for the low-index facets. Coverage

calculations were done for up to 5 COs on the surface. In most facets, the subsequent binding energy of the fifth CO become positive, which indicates that a saturated CO coverage had been reached.

3 Results and Discussion

3.1 Surface Energy Under Lattice Strain

Fig 1 (top) shows the surface energy of Ni as a function of lattice strain. For all three metals, when no strain is applied, (111) is the most stable facet relative to the other 11 facets considered. For elastic strains greater than 1% in magnitude, both compressive and tensile strain tend to decrease the surface energies of all 12 facets for the 3 metals. Overall, the surface energies of most stepped surfaces were found to decrease more than terraces with both tensile and compressive strain. The energy changes of (332) generally decreases faster than most facets under compressive strain, followed by (322). Both of these facets are stepped surfaces with a large distance of at least 10\AA between steps. Kinked surfaces such as the (221) or (321) show similar behavior as stepped surfaces.

The changes in facet stability from lattice strain can be rationalized from surface atom displacements. Figure 1 (bottom) shows the atom displacement for the top-most surface atom along the z -direction (perpendicular to the slab) upon the application of strain. For all facets, compressive strain leads to an upward displacement away from the subsurface of a slab, while tensile strain leads to downward displacement towards the subsurface of a slab. Figure 2 shows the vector displacements of the surface atoms for Ni(111), (211), (322) and (311). We observe that for (111) surfaces and other terrace surfaces, the relative surface atom displacement is very small with response to both compressive and tensile lattice strain, as opposed to the stepped surfaces, which show a greater sensitivity to lattice strain and will relax atoms in larger displacements.

Surface atoms are highly undercoordinated. In particular, the stepped surface atoms on stepped surfaces are notably undercoordinated. They therefore stabilized through decreases in their bond lengths with coordinating atoms. Figure 2, which illustrate the atom displacements associated with the application of strain. Upon application of compressive strain, the bond lengths between the stepped atom and nearby surface atoms are decreased. Upon application of tensile strain, the bond lengths between the stepped atom and the subsurface layer decreases. When lattice strain is present, we find that the relaxed surface structures manage to compensate largely for the uncoordinated of these stepped surface atoms. This helps reduce the surface energies of stepped surfaces more dramatically than terrace surfaces. In general, the amount of surface energy stabilization is quadratically proportional to the amount of surface atom z -displacement that shifts in response to lattice strain as shown in 1.

Figure 3 shows the Wulff shapes for Ni from -3% compressive strain through +4% tensile strain. Supplementary Figures S5 and S6 show the corresponding results for Cu and Pt. Stepped facets are indicated by a netted pattern. Consistent with the trends in surface energy as a function of strain, we find an increase in area fraction of higher index, stepped facets with increasing strain on all 3 metals. For Ni, we observe (332) facets under great strain in either direction. (322) and (310) are observed to be stabilized under moderate levels of strain. Ni(211) appears with 4% tensile strain. For Cu, the (311) and to some extent the (310) increases in area fraction under tensile strain, and for compressive strain, the (322) and (332) facets are stabilized. Finally, in the Pt Wulff shape, (321) dominates under tensile strain cases and (110) under compressive strain. Pt(111) does not appear in any Pt Wulff shape above +1% tensile strain, whereas Pt(100) is stable all strain values.

The stabilization of stepped sites with strain can also be quantified through the step density as a function of strain, shown in Figure 4. In all three metals, both tensile and compressive strains beyond 1-2% gives a marked increase in step site density. This shows that a small amount of strain can give rise to an appreciable increase in step sites. A 3% strain in either direction will increase the step site density by at least 15% on Pt, 30% in Ni and a doubling of step site density in Cu.

Contrary to the general trends of the stabilization of steps with strain, there is a slight decrease in step-site density at 1% compressive lattice strain on Cu. This is due to the decrease in (311) area fraction, a facet with relatively dense coverage of step sites, in favor of a more modestly kinked (310) facet. These facets account for 5% of the entire Cu Wulff shape. Likewise, the Pt step-site density has a minimum at around 1% tensile strain, despite a lower area fraction for both (100) and (111) facets; we attribute this to decrease in area coverage of densely-stepped facets in favor of slightly less stepped facets, which account for about 5% of the surface of the entire Pt Wulff shape.

Lattice strain can therefore be exploited to fabricate highly stepped surfaces, for example, in overlayer structures where the components have mismatched lattice constants. This principle has been exploited in InGaAs island formation on GaAs substrates³⁶, and in Si/oxide wafers. In the latter case, rapid heating and cooling led to the formation of dislocations on the Si overlayer, which relieved planar stresses that would have been present on a planar surface.

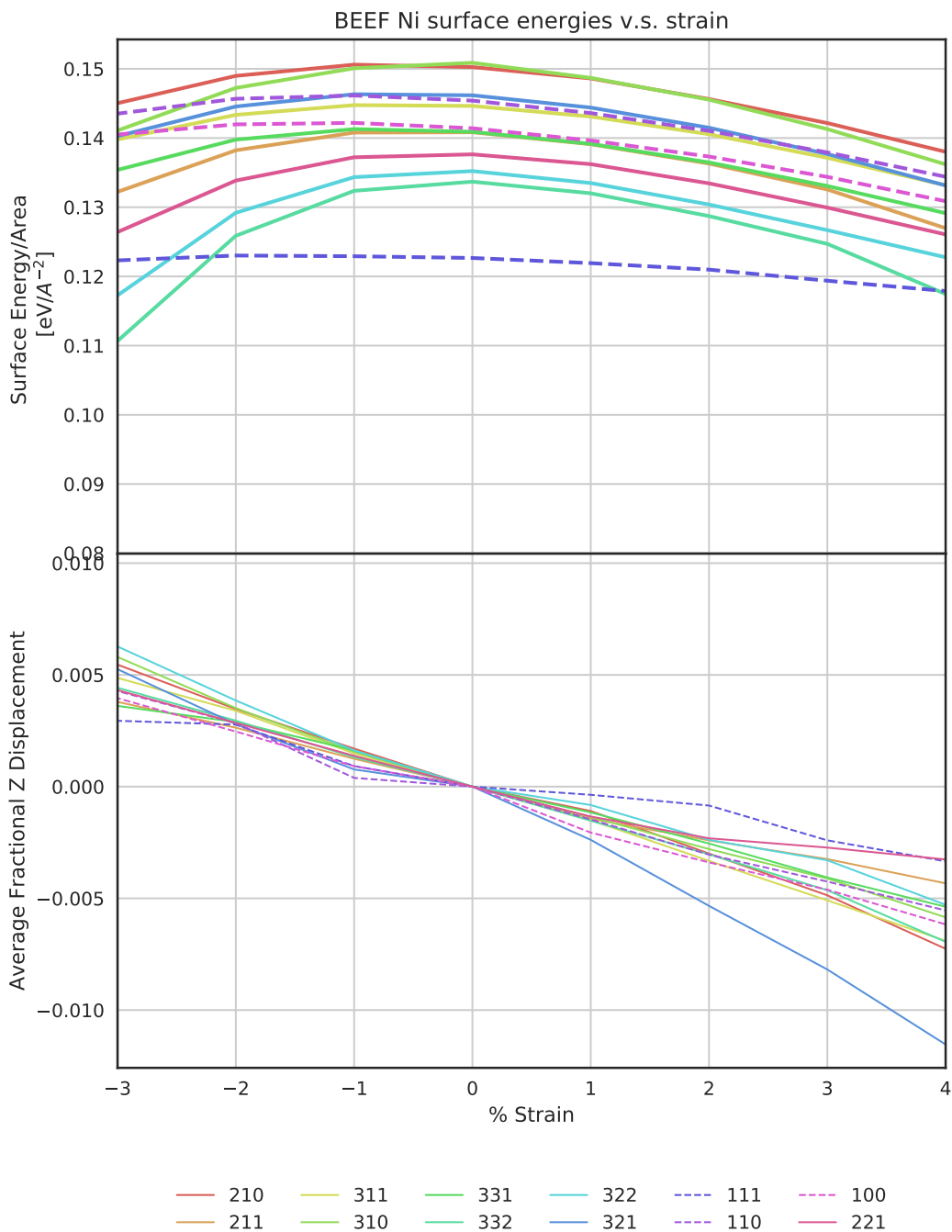


Figure 1: Surface energy vs Lattice Strain on Ni surfaces, as determined with the BEEF functional. Top: Surface Energies; Bottom: The corresponding z -displacement of the topmost atom(s) in the slabs

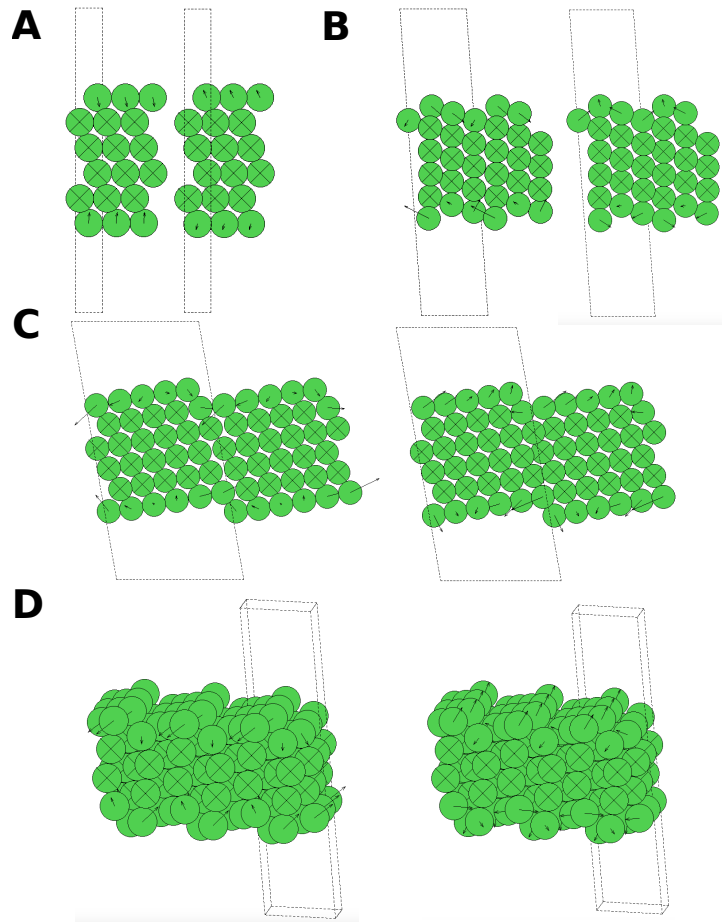


Figure 2: Surface Atom Displacements for varying facets: +2% lattice strain conditions (left) and -2% lattice strain (right). A. Ni(111), B. Ni(211), C. Ni(322), D. Ni(321)

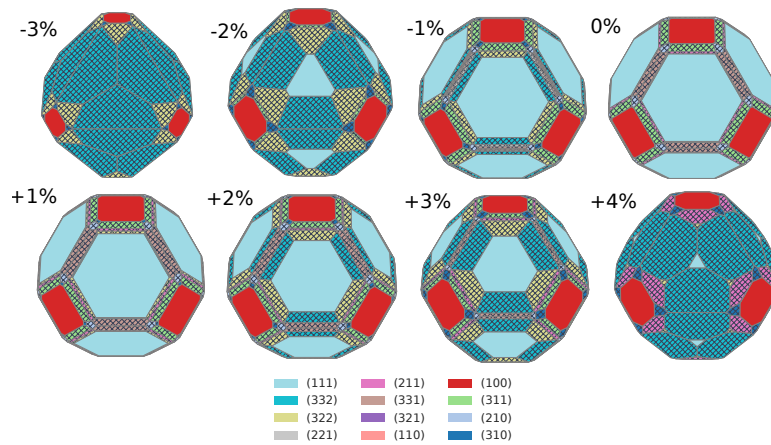


Figure 3: Nickel Wulff shape showing equilibrium crystal shapes according to calculated facet surface energies from BEEF. Stepped sites are indicated by a hatched pattern

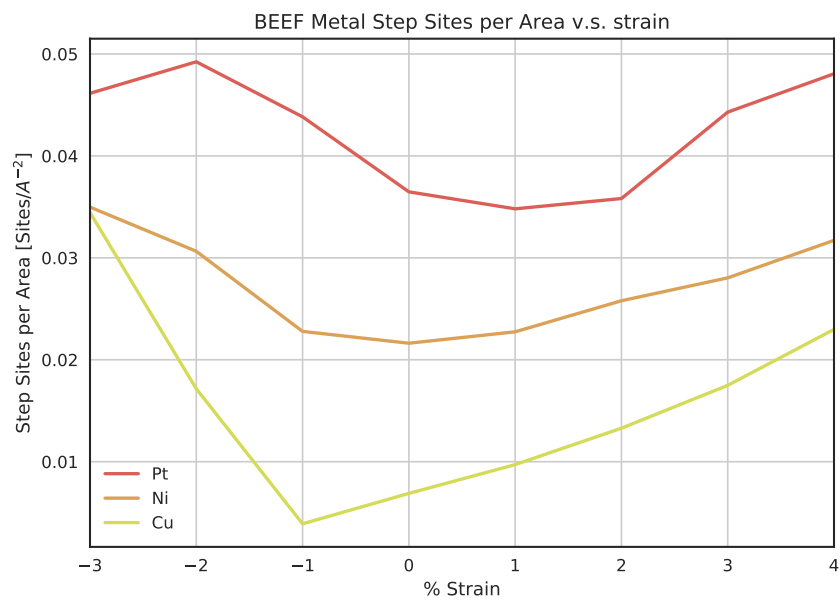


Figure 4: BEEF optimized Step Site Density v.s. Strain

3.2 Surface Stabilization Under CO Environment

In addition, we investigated the effects of CO adsorbates on surface energies. A previous work has explored adsorbate-induced stabilization of facets on Au³⁷; due to the weak CO interaction on Au surfaces, a CO environment did not change the particle shape of Au appreciably. Here, we focus on Cu, Ni, and Pt, all of which bind CO more strongly than Au.

The surface energy of a facet in the presence of adsorbates is given by

$$\gamma_{hkl}^{int} = \gamma_{hkl} + \frac{E^{N,covered} - E^{clean} - N\Delta\mu_{CO}}{A_{tot}}, \quad (4)$$

where $E^{N,covered}$ is the energy of a slab covered with N adsorbates, E^{clean} is the energy of the clean slab, and $\Delta\mu_{CO}$ is the change in chemical potential of CO gas over CO partial pressure:

$$\Delta\mu_{CO} = \mu_{CO} - \mu_{o,CO}(273K, 1\text{bar}) = k_B T \ln\left(\frac{p}{p_o}\right) \quad (5)$$

The stronger a facet binds CO, the more its surface energy is stabilized in the presence of CO. We then considered a range of $\Delta\mu_{CO}$ between -0.9 to 0.1eV, which corresponds to a range in CO partial pressure between 9.3×10^{-16} bar (beyond an ultrahigh vacuum limit) and around 50 bars. The CO coverages were given by: $\theta_{CO} = n_{CO}/M$, where M is the number of surface atoms.

Figure 5 shows, as an example, how surface energy and CO coverage changes with CO partial pressure on Ni(211). The color shading under the black line indicates the most stable CO coverage under the given CO pressure. In general, a higher CO partial pressure leads to higher CO coverages. The corresponding surface energies for the remaining Ni, Pt, and Cu facets are shown in SI Figures 7 to 35. Since Ni and Pt bind CO strongly, even at the lowest CO chemical potential considered (corresponding to 9.3×10^{-16} bar), the majority of Ni and Pt facets will still have a finite coverage of $\theta = 0.38 - 0.5$. Cu, which binds weaker, will still have up to 0.5 coverage on several of its stepped facets, starting at moderate pressures of about 1×10^{-5} to 1×10^{-3} bar.

In Figure 6, we illustrate the sensitivity of the relative stability of surface facets to a CO environment through a comparison of Wulff shapes under ideal vacuum conditions to those under a chemical potential of -0.5 eV, corresponding to a very small CO partial pressure of 4.4×10^{-9} bar. Even at such a low CO pressure, the equilibrium Wulff shapes are dramatically affected by the presence of CO. Ni and Cu have a clear increase in area coverage of stepped facets, which are indicated by a hatched pattern. Ni's Wulff shape evolves to include more (221) and (211) facets, while Cu's Wulff shape changes to contain more (310) facets. However, Pt shows significant area fractions of both terrace and stepped facets under both ideal and low CO pressure conditions.

The sensitivity of the Wulff shapes and corresponding facet distribution to variations pressure is illustrated for Ni as an example in Figure 7. The chemical potential is varied between -0.9 to -0.1eV, corresponding to a variation of CO partial pressure between 9.3×10^{-16} bar to 50 bars. The corresponding figures for Pt and Cu are shown in Supplementary Figure S36. In general, the particle shapes of Ni and Cu change significantly more with pressure than Pt, and this effect can be rationalized through the evolution of step site densities. The step site density of all three metals as a function of CO partial pressure are shown in Figure 8. We find that, for Ni and Cu, the step site density generally increases as partial pressure of CO increases. Interestingly, the step site density of Pt remains essentially unchanged as CO partial pressure increases. The strong binding energy of CO on Pt allows for its terrace facets to have a higher saturation coverage compared to Ni and Cu. This causes the surface energy stabilization of stepped facets over terrace facets to be smaller for Pt than for Ni and Cu.

The findings on Cu are in line with recent experimental reports. The reconstruction of polycrystalline copper surfaces was observed under a CO atmosphere and were characterized with surface-enhanced Raman and attenuated total internal reflection Fourier-transform infrared spectroscopies. An increase in CO pressure led to a strengthening of the peak associated with CO adsorption on stepped sites relative to the one associated with terrace sites, which suggests that a higher CO coverage encourages the formation of uncoordinated sites³⁸.

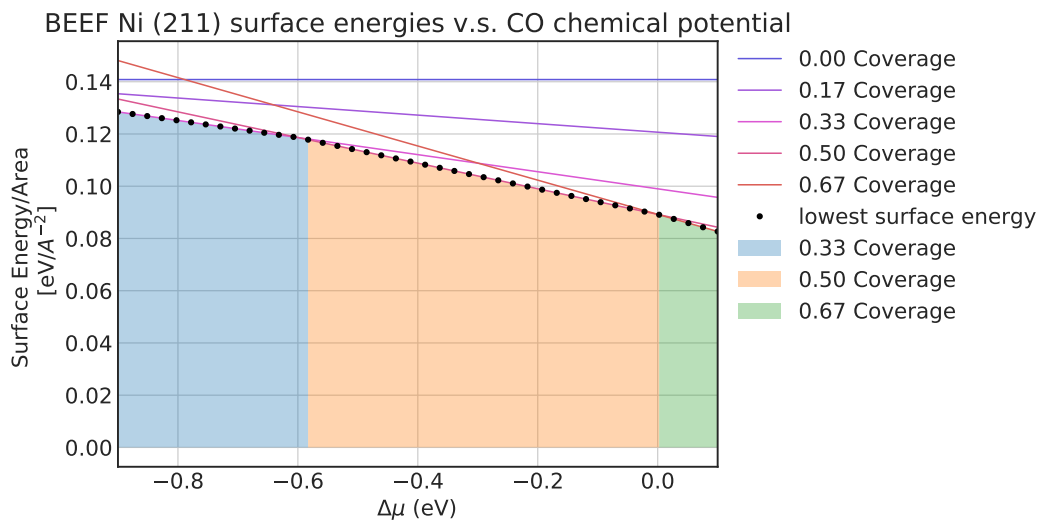


Figure 5: Surface energy changes with CO partial pressure on Ni (211). $\Delta\mu$ corresponds to CO chemical potential with regards to its partial pressure levels: -0.9eV is a CO partial pressure of around 9.3×10^{-16} bar and 0.1eV is a pressure of around 50 bars. Color shading signifies shifts in CO coverages through the partial pressure levels.

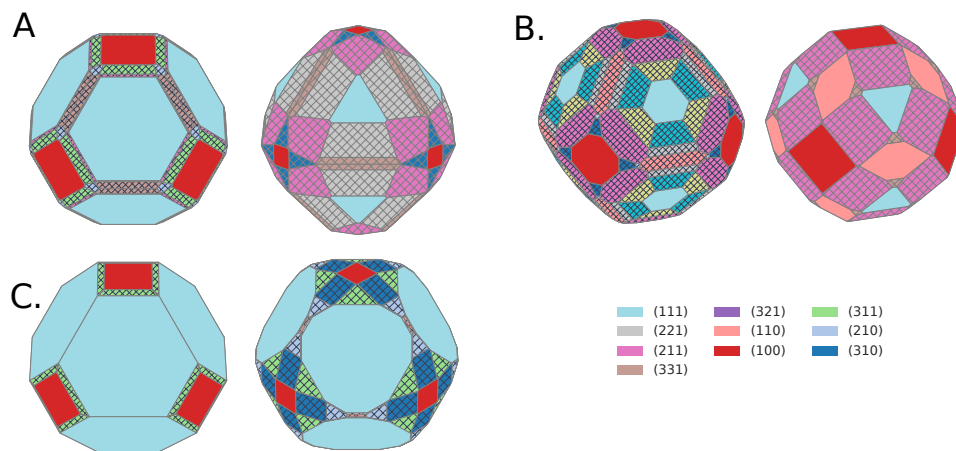


Figure 6: Wulff Shape Comparison: Left: ideal Wulff shapes for each metal, Right: Wulff shapes under a CO partial pressure of 4.44×10^{-9} bars. A. Ni; B. Pt; C. Copper. Stepped facets are indicated by a hatched pattern.

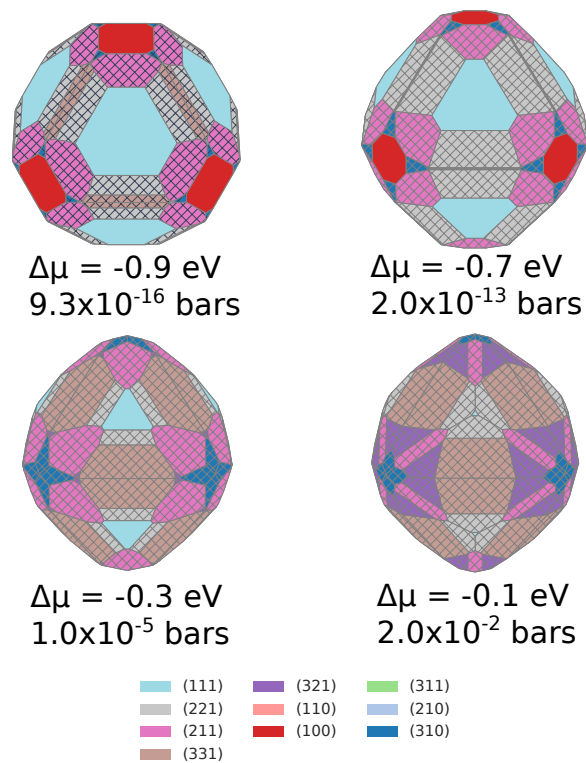


Figure 7: Wulff Shape Evolution as a function of CO Partial Pressure for Ni. As CO partial pressure increases, the area coverage of stepped facets increase.

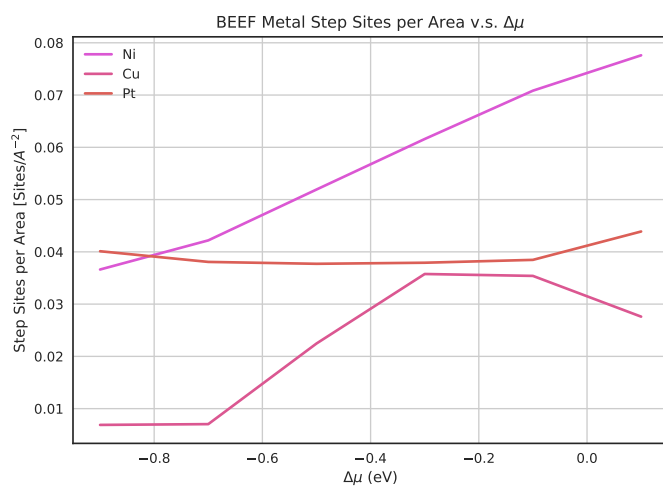


Figure 8: Mean step site density over CO Partial Pressure. As CO partial pressure increases, stepped facets appear more frequent on Cu. Stepped facets are indicated by a hatched pattern.

4 Conclusions

Using DFT calculations of surface energies and the corresponding equilibrium Wulff shapes, we find both lattice strain and CO environment to have appreciable effects on the surface stability of transition metal surfaces. We find that stepped facets are stabilized by both compressive and tensile strain. CO adsorption tends to stabilize stepped facets on Cu and Ni, but has a negligible effect on the step density on Pt. We have illustrated these trends with Wulff constructions of nanoparticle shape. The overall effect of strain and adsorbates on catalytic activity therefore comes from the interplay of electronic structure effects and facet stability. These insights suggest that studying simple low index terraces may not be sufficient to elucidate the underlying reaction mechanisms on catalyst surfaces, and they should also be considered in the design of new catalysts.

5 Competing Financial Interests

The authors declare no competing financial interests.

6 Supporting Information Available

All data used to reproduce figures presented in the paper are provided in tables. Additionally, datatables describing Ni, Cu, and Pt facet surface energy changes as well as surface atom displacement with respect to elastic lattice strain are included. We provided a demonstration of the linear-fit method in determining surface energy on Ni(111). We defined the surface step site density used in this paper in the SI. We provided a comparison of the surface energies obtained through our calculations with other theoretical works, namely Crystalium. Our PBE calculation results describing the changes in surface energy versus lattice strain are provided. Supplemental figures describing surface energy changes with respect to CO partial pressure are also included for Ni, Cu, and Pt. Additional Wulff shapes evolution of Cu and Pt through lattice strain and CO partial pressures are presented in the supplement.

Acknowledgements

This material is based upon work performed by the Joint Center for Artificial Photosynthesis, a DOE Energy Innovation Hub, supported through the Office of Science of the U.S. Department of Energy under Award Number DE-SC0004993. This research used resources of the National Energy Research Scientific Computing Center, a DOE Office of Science User Facility supported by the Office of Science of the U.S. Department of Energy under Contract No. DE-AC02-05CH11231. M.T.T recognizes a Graduate Research Fellowship from the National Science Foundation under Grant No. DGE-114747.

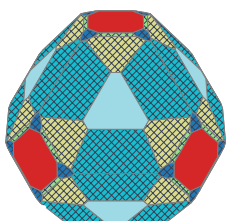
References

- [1] Kitchin, J. R.; Nørskov, J. K.; Barteau, M. A.; Chen, J. G. Role of Strain and Ligand Effects in the Modification of the Electronic and Chemical Properties of Bimetallic Surfaces. *Phys. Rev. Lett.* **2004**, *93*, 156801.
- [2] Mavrikakis, M.; Hammer, B.; Nørskov, J. K. Effect of Strain on the Reactivity of Metal Surfaces. *Phys. Rev. Lett.* **1998**, *81*, 2819–2822.
- [3] Lim, F. C. H.; Zhang, J.; Jin, H.; Sullivan, M. B.; Wu, P. A density functional theory study of CO oxidation on Pd-Ni alloy with sandwich structure. *Applied Catalysis A: General* **2013**, *451*, 79–85.
- [4] Amakawa, K. et al. How Strain Affects the Reactivity of Surface Metal Oxide Catalysts. *Angew. Chem. Int. Ed.* **2013**, *52*, 13553–13557.
- [5] Gan, L.; Yu, R.; Luo, J.; Cheng, Z.; Zhu, J. Lattice Strain Distributions in Individual Dealloyed PtFe Catalyst Nanoparticles. *J. Phys. Chem. Lett.* **2012**, *3*, 934–938.
- [6] Kubicek, M.; Cai, Z.; Ma, W.; Yildiz, B.; Hutter, H.; Fleig, J. Tensile Lattice Strain Accelerates Oxygen Surface Exchange and Diffusion in La_{1-x}Sr_xCoO₃ Thin Films. *ACS Nano* **2013**, *7*, 3276–3286.
- [7] Ouyang, G.; G.Zhu, W.; Q.Sun, C.; M.Zhu, Z.; Z.Liao, S. Atomistic origin of lattice strain on stiffness of nanoparticles. *Physical Chemistry Chemical Physics* **2010**, *12*, 1543–1549.

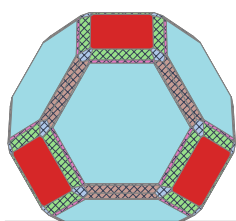
- [8] Moseley, P.; Curtin, W. A. Computational Design of Strain in CoreShell Nanoparticles for Optimizing Catalytic Activity. *Nano Lett.* **2015**, *15*, 4089–4095.
- [9] Suzuki, S.; Onodera, T.; Kawaji, J.; Mizukami, T.; Yamaga, K. Effect of support materials on platinum lattice strain and its oxygen reduction activity. *Applied Catalysis A: General* **2012**, *427428*, 92–97.
- [10] Wang, H. et al. Direct and continuous strain control of catalysts with tunable battery electrode materials. *Science* **2016**, *354*, 1031–1036.
- [11] Yang, J.; Chen, X.; Yang, X.; Y. Ying, J. Stabilization and compressive strain effect of AuCu core on Pt shell for oxygen reduction reaction. *Energy & Environmental Science* **2012**, *5*, 8976–8981.
- [12] Yoshimoto, Y.; Tsuneyuki, S. First-principles study on the strain effect of the Cu(001)-c(22)N self-organized structure. *Applied Surface Science* **2004**, *237*, 274–278.
- [13] Zhang, S.; Zhang, X.; Jiang, G.; Zhu, H.; Guo, S.; Su, D.; Lu, G.; Sun, S. Tuning Nanoparticle Structure and Surface Strain for Catalysis Optimization. *J. Am. Chem. Soc.* **2014**, *136*, 7734–7739.
- [14] Kuo, C.-H.; Lamontagne, L. K.; Brodsky, C. N.; Chou, L.-Y.; Zhuang, J.; Sneed, B. T.; Sheehan, M. K.; Tsung, C.-K. The Effect of Lattice Strain on the Catalytic Properties of Pd Nanocrystals. *ChemSusChem* **2013**, *6*, 1993–2000.
- [15] Zhang, J.-M.; Zhang, M.-Y.; Xu, K.-W. Missing row reconstruction on three low index surfaces of ten FCC metals. *Cryst. Res. Technol.* **2009**, *44*, 275–280.
- [16] Klink, C.; Olesen, L.; Besenbacher, F.; Stensgaard, I.; Laegsgaard, E.; Lang, N. D. Interaction of C with Ni(100): Atom-resolved studies of the “clock” reconstruction. *Phys. Rev. Lett.* **1993**, *71*, 4350–4353.
- [17] Jensen, F.; Besenbacher, F.; Laegsgaard, E.; Stensgaard, I. Surface reconstruction of Cu(110) induced by oxygen chemisorption. *Phys. Rev. B* **1990**, *41*, 10233–10236.
- [18] Niehus, H. Surface reconstruction of Cu (111) upon oxygen adsorption. *Surface Science* **1983**, *130*, 41–49.
- [19] Almora-Barrios, N.; Novell-Leruth, G.; Whiting, P.; Liz-Marzn, L. M.; Lopez, N. Theoretical Description of the Role of Halides, Silver, and Surfactants on the Structure of Gold Nanorods. *Nano Lett.* **2014**, *14*, 871–875.
- [20] Matsushima, H.; Taranovskyy, A.; Haak, C.; Grnder, Y.; Magnussen, O. M. Reconstruction of Cu(100) Electrode Surfaces during Hydrogen Evolution. *J. Am. Chem. Soc.* **2009**, *131*, 10362–10363.
- [21] Matsushima, H.; Haak, C.; Taranovskyy, A.; Grnder, Y.; Magnussen, O. M. In situ video STM studies of the hydrogen-induced reconstruction of Cu(100): potential and pH dependence. *Phys. Chem. Chem. Phys.* **2010**, *12*, 13992–13998.
- [22] Giannozzi, P. et al. QUANTUM ESPRESSO: a modular and open-source software project for quantum simulations of materials. *J. Phys.: Condens. Matter* **2009**, *21*, 395502.
- [23] Larsen, A. H. et al. The atomic simulation environmenta Python library for working with atoms. *J. Phys.: Condens. Matter* **2017**, *29*, 273002.
- [24] Wellendorff, J.; Lundgaard, K. T.; Mgelhj, A.; Petzold, V.; Landis, D. D.; Nrskov, J. K.; Bligaard, T.; Jacobsen, K. W. Density functionals for surface science: Exchange-correlation model development with Bayesian error estimation. *Phys. Rev. B* **2012**, *85*, 235149.
- [25] Perdew, J. P.; Burke, K.; Ernzerhof, M. Generalized Gradient Approximation Made Simple. *Phys. Rev. Lett.* **1996**, *77*, 3865–3868.
- [26] Tran, R.; Xu, Z.; Radhakrishnan, B.; Winston, D.; Sun, W.; Persson, K. A.; Ong, S. P. Surface energies of elemental crystals. *Scientific Data* **2016**, *3*, 160080.
- [27] Monkhorst, H. J.; Pack, J. D. Special points for Brillouin-zone integrations. *Phys. Rev. B* **1976**, *13*, 5188–5192.
- [28] Ong, S. P.; Richards, W. D.; Jain, A.; Hautier, G.; Kocher, M.; Cholia, S.; Gunter, D.; Chevrier, V. L.; Persson, K. A.; Ceder, G. Python Materials Genomics (pymatgen): A robust, open-source python library for materials analysis. *Computational Materials Science* **2013**, *68*, 314–319.

- [29] Greaves, G. N.; Greer, A. L.; Lakes, R. S.; Rouxel, T. Poisson's ratio and modern materials. *Nature Materials* **2011**, *10*, 823–837.
- [30] Sun, W.; Ceder, G. Efficient creation and convergence of surface slabs. *Surface Science* **2013**, *617*, 53–59.
- [31] Zhang, W.-B.; Chen, C.; Zhang, S.-Y. Equilibrium Crystal Shape of Ni from First Principles. *J. Phys. Chem. C* **2013**, *117*, 21274–21280.
- [32] Kappes, B. B.; Leong, G. J.; Gilmer, G. H.; Richards, R. M.; Ciobanu, C. V. Metallic nanocrystals synthesized in solution: a brief review of crystal shape theory and crystallographic characterization. *Crystal Research and Technology* **2015**, *50*, 801–816.
- [33] Li, L.; Abild-Pedersen, F.; Greeley, J.; Nørskov, J. K. Surface Tension Effects on the Reactivity of Metal Nanoparticles. *J. Phys. Chem. Lett.* **2015**, *6*, 3797–3801.
- [34] Goedecker, S. Minima hopping: An efficient search method for the global minimum of the potential energy surface of complex molecular systems. *The Journal of Chemical Physics* **2004**, *120*, 9911–9917.
- [35] Shi, C.; Chan, K.; Yoo, J. S.; Nørskov, J. K. Barriers of Electrochemical CO₂ Reduction on Transition Metals. *Org. Process Res. Dev.* **2016**, *20*, 1424–1430.
- [36] Snyder, C. W.; Orr, B. G.; Kessler, D.; Sander, L. M. Effect of strain on surface morphology in highly strained InGaAs films. *Phys. Rev. Lett.* **1991**, *66*, 3032–3035.
- [37] Barmbaris, G. D.; Remediakis, I. N. Dependence on CO adsorption of the shapes of multifaceted gold nanoparticles: A density functional theory. *Phys. Rev. B* **2012**, *86*, 085457.
- [38] Gunathunge, C. M.; Li, X.; Li, J.; Hicks, R. P.; Ovalle, V. J.; Waegle, M. M. Spectroscopic Observation of Reversible Surface Reconstruction of Copper Electrodes under CO₂ Reduction. *J. Phys. Chem. C* **2017**, *121*, 12337–12344.

TOC Graphic



Elastic Lattice Strain



CO Adsorption

